A comprehensive analysis of electron emission from a-Si:H/Al2O3 at very low energies

Janina Löffler, Mohamed Belhaj, Nenad Bundaleski, Juan J Diaz Leon, Jonathan Thomet, Samira Frey, Christophe Ballif, Nicolas Wyrsch

A comprehensive analysis of electron emission from a-Si:H/Al2O3 at low energies

A comprehensive analysis of electron emission from a-Si:H/Al_2O_3 at low energies

Janina Löffler[1,2], Mohamed Belhaj[3], Nenad Bundaleski[4], Juan J. Diaz Leon[5], Jonathan Thomet[1], Samira Frey[1], Christophe Ballif[1,5], Nicolas Wyrsch[1]

[1]Photovoltaics and Thin-Film Electronics Laboratory, Institute of Electrical and Microengineering (IEM), Ecole Polytechnique Fédérale de Lausanne (EPFL), Neuchâtel, Switzerland, [2]HES-SO Valais-Wallis, HES-SO University of Applied Sciences and Arts Western Switzerland, [3]ONERA-DPHY, 2 avenue E. Belin, 31055 Toulouse, France, [4]CEFITEC, Departamento de Física, Faculdade de Ciencias e Tecnologia, Universidade Nova de Lisboa, Quinta da Torre, 2829e516 Caparica, Portugal, [5]CSEM Sustainable Energy Center, Jaquet-Droz 1, 2002 Neuchâtel, Switzerland

E-mail: janina.loffler@hevs.ch

November 2022

Abstract. Recently developed microchannel plates based on amorphous silicon offer potential advantages with respect to glass based ones. In this context, secondary electron emission at very low energies below 100 eV has been studied for relevant materials for these novel devices. The aim of this work was to quantify the low energy electron emission - secondary emission and elastic scattering - from amorphous silicon and alumina and the dependence of the emission energy distribution on the primary electron energy, which was previously unknown. Secondary emission and energy distribution were both modelled and measured using equipment particularly designed for this energy range. The effects of roughness, angle of incidence and surface composition were analysed. We show crossover energies as well as the angular dependence of electron emission from amorphous silicon and alumina, with a maximum experimental emission yield value of 2 and 2.8, respectively, at an incident angle of 75°. A parameterization for the energy dependence of the emission energy spectrum at low energies was derived. This extensive analysis is fundamental for a comprehensive understanding of the performance of amorphous silicon-based microchannel plate detectors. It provides a complete model for secondary electron emission for a detailed description of the detector operation. The present results thus set the basis for a simulation framework, which is an essential element to increase the performance of these detectors and enable further developments.

Keywords: secondary electron emission, electron emission energy, a-Si:H, Al_2O_3, high secondary electron emissive layers, microchannel

Submitted to: *J. Phys. D: Appl. Phys.*

1. Introduction

Secondary electron emission (SEE) is a fundamental physical phenomenon behind the working principle of electron multipliers. The latter represent a wide class of devices that provide sensing of low intensity radiation, down to the detection of single particles. An energetic electron impinging a dynode of a discrete electron multiplier produces several secondary electrons, which are then accelerated towards the next dynode. In the following collisions the electrons are further multiplied, resulting in an electron avalanche, eventually providing a current pulse per each particle impinging the detector.

We see from the previous example that the total electron yield (TEY), defined as the average number of electrons emitted per incident primary electron, is of extreme importance in electron multipliers. More precisely, dependence of the TEY on primary electron energy plays an essential role in their design and operation. The second important feature of SEE, from the perspective of electron multipliers, is the energy distribution of emitted electrons, since the initial electron energy determines both the electron trajectory and its impinging energy onto the next dynode.

Glass based microchannel plates (MCPs) are electron multipliers with high spatial resolution of the order of tens to hundreds of µm that were developed in the 1970s (Ladislas Wiza (1979)). However, both the collection efficiency, i.e. the probability that a particle will enter a channel, and temporal resolution of MCPs are limited as channel geometries and the vertical conductivity are largely fixed. State-of-the-art clean room processes have recently enabled fabrication of a novel electron multiplier with high resolution based on hydrogenated amorphous silicon (a-Si:H) (Franco et al. (2014)) with the potential to overcome the inherent limitations of MCPs. Amorphous silicon based microchannel plates (AMCPs) can be integrated monolithically and the vertical conductivity can be adjusted through doping. AMCP channel spacing and diameters can be customized down to narrow diameters below 3 µm (Löffler et al. (2018)). During the fabrication of AMCPs, channels with walls having different surface morphologies can be realized, which could additionally increase TEY. Another strategy in improving MCP performances is to deposit high TEY materials on the inner walls using atomic layer deposition (ALD), which is known to make conformal coatings even over nanostructured surfaces (Elam et al. (2006)). Although layers with higher secondary electron emissivity can be deposited by ALD, Al_2O_3 layers are particularly suitable for this purpose due to the well-established and broadly available technology.

From the gain of AMCPs, the average number of collisions inside the channel has been calculated by Löffler et al. (2018). With a number of collisions of at least 6 and a bias voltage of 500 V, secondary electrons that are emitted with few eV gain an average of about 80 eV. An average energy of 40 eV has been found by Frey et al. (2019) for electrons that exit the channels. Knowing that electron paths between two collisions inside the channel become even shorter for high aspect ratio AMCPs with smaller channel diameters, electrons inside those channels hardly gain kinetic energies above 100 eV. Therefore, designing AMCPs with the most suitable architecture requires

detailed understanding of SEE from this particular material in the energy range which is rarely investigated, i.e. below 100 eV. Thus, the present analysis is key to understanding the full potential and the limits of AMCPs, and to be able to assess their performance as a function of device geometries and surface morphology of the channels.

Low energy electron-matter interaction is a subject of great uncertainty with measurements of the TEY at 0 eV being controversial, as discussed by Andronov et al. (2013). Most of the commonly used physical models are inadequate for electron energies below 50 eV (Kieft and Bosch (2008)), implying that TEY modelling is also unreliable. While more accurate theories for low energy electron scattering are still to be explored, we have to rely on TEY measurements in this energy range. The latter, being a challenge on their own, have been performed mainly for materials that are used in space technologies by Balcon et al. (2012) including for metals such as Cu by Schulte et al. (2020), Ag, Au and crystalline silicon (c-Si) by Pierron et al. (2017). Further experimental difficulties originate when performing such measurements on non-conductive surfaces prone to surface charging.

In this paper, we extended the low energy SEE studies to a-Si:H and ALD-deposited Al_2O_3. A setup presented by Belhaj et al. (2010), highly suitable for TEY measurements from non-conductive surfaces, was used to determine the previously unknown TEY of a-Si:H and Al_2O_3 surfaces for energies below 100 eV. In addition, the energy spectra of emitted electrons from the same surfaces for primary electron energies below 200 eV were measured using a setup particularly designed for such purposes by Villemant et al. (2017). The importance of this investigation is in the ability to follow the change of the overall spectra (e.g. the relative contribution of elastically backscattered electrons) with the primary electron energy. Furthermore, the study can be extended to other high TEY coatings, such as MgO and composite structures.

In parallel to the experimental investigations, we used Monte Carlo (MC) simulators and analytical models. Furthermore we developed an original approach to consider the influence of surface morphology on TEY and applied it to the materials of interest. This allowed us to evaluate their capabilities in describing SEE phenomena at low primary energies in the case of a-Si:H and Al_2O_3 and thus their utility potential for future AMCP simulators.

2. Materials and methods

2.1. Sample preparation

The thin films of a-Si:H and Al_2O_3 used in this study were deposited on HF cleaned polished c-Si wafer substrates by means of plasma enhanced chemical vapor deposition (PECVD) and ALD, respectively. Two different procedures were used for the deposition of a-Si:H, yielding distinct surface morphologies i.e. roughness. Some of the a-Si:H films were additionally coated by Al_2O_3.

The film thickness of both resistive materials studied here was kept as thin as

possible in order to minimize charging problems, yet thick enough to measure electron emission from the film itself. Since the minimal film thickness is given by the secondary electron escape depth of few nm (Fitting et al. (2001)), all a-Si:H layers in this study were aimed to be about 15-20 nm.

The PECVD setup and deposition recipe of a-Si:H were described in detail by Franco et al. (2014). Rough surfaces were produced using the aforementioned recipe applied for the deposition of AMCP layers. Briefly said, the former deposition recipe is optimized for low intrinsic stress for the deposition of thick layers, resulting in a corrugated surface, when deposited as a thin film of few nm. Additionally, a procedure optimized for surface flatness was used to deposit a second set of samples. By comparing the SEE properties of the two types of films, we were able to estimate the influence of surface morphology on the overall secondary electron emission behaviour.

Al_2O_3 was deposited in an Oxford FlexAl ALD setup using a mixture of Trimethylaluminum ($Al_2(CH_3)_6$) and water. The thickness of the deposited films was about 5 nm on both the corrugated a-Si:H surface and the substrate surface (used as the reference sample).

Thickness of thin films was measured with an ellipsometer and interpreted using the dispersion model developed by Cauchy (1830).

2.2. Surface characterization

The two main characteristics of surfaces, i.e. their topography and their chemical composition, govern the process of secondary electron emission. We analysed the topography using an atomic force microscope (AFM) Bruker VT-102-2. The data analysis was performed using Gwyddion v.2.58. Surface chemical composition analysis was performed by means of X-ray photoelectron spectroscopy (XPS). The XPS setup consists of a monochromatic X-ray gun with Al anode, providing a photon energy of 1486.7 eV, and a hemispherical electron energy spectrometer. The spectra were acquired in the fixed analyzer transmission mode with the pass energy of 200 eV. The line intensities were determined after removal of the background of Shirley type. The composition was determined using appropriate sensitivity factors, under the assumption of in-depth uniform samples. Hydrogen concentration was not measured. In general, it is about 5-20% in a-Si:H, with a hydrogen rich surface (Blayo and Drévillon (1992)). Hydrogen on the surface can be present as adsorbed H_2O and is usually removed by annealing in AMCPs, as described by Franco (2014).

2.3. SEE measurements

SEE measurements were performed on the ALCHIMIE and DESSE facilities located at Onera, both providing a base pressure of 10^{-10} mbar.

The TEY was measured at ALCHIMIE/DEESSE using a charge collection method with a pulsed electron beam, which has been proven to avoid charging effects and consequently enables an accurate measurement of the electron emission yield of insulators at low

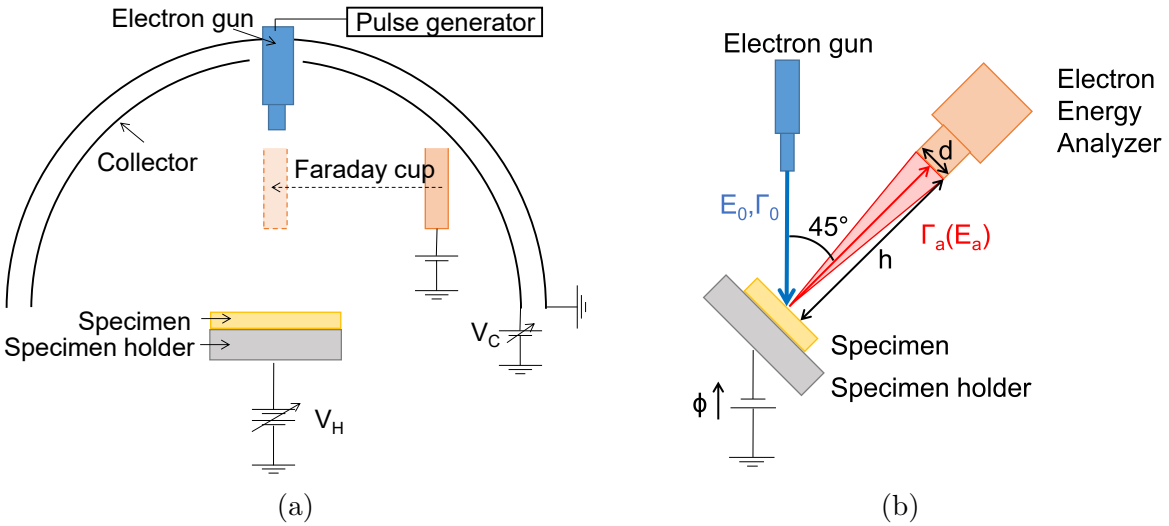

Figure 1: (a) Experimental setup for total electron emission yield measurements. The sample was tilted at various angles for an electron beam incidence from 0° up to 75°, relative to the surface normal. (b) Electron energy analyzer for characterization of the emission energy distribution. The sample was mounted at 45° with respect to the incident beam. This analyzer was calibrated for low energies by Villemant et al. (2017).

energies. The method and setup employed in this work were described in detail by Belhaj et al. (2010). The schematic of the setup is presented in figure 1a. The incident electron angle was varied from normal incidence (0°) up to 75°. The incident electron energies ranged from 10 to 1000 eV. The primary electron current was measured by a Faraday cup that was introduced between the electron gun and the sample holder. For each incident energy, 10 pulses of 6 ms and a current in the nA range were delivered. The TEY was calculated as the ratio between the sample charge and the incident charge.

The energy distribution of the emitted electrons was measured for electron irradiation with different incident energies using the hemispherical electron energy analyzer Omicron EA 125 of DEESSE, suitable for an energy range from few eV to 2 keV. The energy spectrometer was working in the fixed analyser transmission regime, with the electron pass energy of 200 eV. The schematic of the setup inside the vacuum chamber is shown in figure 1b. The samples were tilted by 45° with respect to the incident beam with monochromatic energy E_0 and the emission energy analyzer was facing the sample plane. The sample was kept at a bias of φ = -11.5 V. For an incident electron energy E_0 and flux Γ_0, electrons with energies E_e in the range from 0 eV to E_0 were emitted from the sample.

The energy E_a recorded at the analyzer was

$$E_a = E_e - e\varphi + (\phi_{sample} - \phi_{spectrometer}) \quad (1)$$

with the elemental charge e and the respective work functions of the sample and the spectrometer, ϕ_{sample} and $\phi_{spectrometer}$. An extensive correction was elaborated for low energy emission spectra measurements by Villemant et al. (2017), as the electron energy

analyzer is typically calibrated for energies higher than 300 eV. Additionally, geometrical constraints due to the limited field of view of the analyzer were taken into account. In summary, the emission spectra were obtained from the recorded spectra $\Gamma_a(E_a)$ at energies E_a with an energy step $\Delta E = 0.2\,\mathrm{eV}$ as follows:

$$N(E_e) = \frac{1}{\sum_{i=1}^{M}\left(\frac{\Gamma_a(E_i)}{H(E_i,\varphi)}\right)} \cdot \frac{\Gamma_a(E_a)}{H(E_e,\varphi)\Delta E}, \tag{2}$$

where $N(E_e)$ is the normalized emission probability at energy E_e. The transfer function $H(E_e,\varphi) = H_T(E_e,\varphi) + H_a(E_a)$ is composed of:

$$H_a(E_a) = \begin{cases} A \cdot \exp\left(\alpha \cdot E_a\right) & \text{for } 0 \le E_a < 124\,\mathrm{eV} \\ 1 & \text{for } E_a \ge 124\,\mathrm{eV}, \end{cases} \tag{3}$$

with $A = 0.0192$ and $\alpha = 0.0319$ for the correction of the analyzer calibration and

$$H_T(E_e,\varphi) = \begin{cases} 1 & \text{for } 0 \le E_e \le 3.25\,\mathrm{eV} \\ \frac{\arctan\left(\frac{d}{2\cdot h}\right)}{\arctan\left(\sqrt{\frac{E_e}{|\varphi|}}\right)} & \text{for } E_e > 3.25\,\mathrm{eV}, \end{cases} \tag{4}$$

with $d = 0.03\,\mathrm{m}$ and $h = 0.03\,\mathrm{m}$ for the geometrical correction.

2.4. SEE modelling

We used existing MC tools, Nebula by van Kessel and Hagen (2020) and Casino by Demers et al. (2011), to model SEE. Nebula was used with the modelling setup described by Löffler et al. (2019). The number of primary electrons in all Nebula results shown throughout this paper was 10^6. The electron-material interaction simulator 3D Casino ver. 3.3 has been used with the standard physical models implemented, using the scattering cross section of the ELSEPA code by Salvat et al. (2005) and the energy loss model by Joy and Luo Joy and Luo (1989). For each incident energy between 10 eV and 300 eV we simulated 3000 electrons for incident angles of 0° and 80°.

In addition, we used a novel simplified approach to model the energy dependence of total electron yield TEY(E) from corrugated surfaces. The latter represents an extension of the earlier work by Bundaleski et al. (2015), in which we predicted TEY(E) from a smooth surface for an arbitrary incident angle from the experimentally measured TEY at normal incidence. As an input to the model TEY(E) from the flat in depth uniform sample measured at normal incidence is used. Then, an AFM image of the actual emitting surface, representing the corrugation function z(x,y), is used to calculate the TEY(E) of that surface. The surface is considered as a mosaic of K flat areas, each having an arbitrary inclination with respect to the surface normal of a perfectly smooth sample. We used the AFM image to determine the local inclination at a point 'i' of the sample surface and the corresponding TEY_i(E) according to the model by Bundaleski et al. (2015). The trajectory of each of the N electrons leaving the surface was monitored. These electrons were ejected from the point 'i', with random outgoing angles following a

cosine distribution. If the number of electrons that managed to leave the surface without colliding with the surface protrusions is M_i, the TEY(E) of the corrugated surface is estimated as

$$\mathrm{TEY(E)} = \sum_{i=1}^{K} \frac{M_i}{N} \cdot \mathrm{TEY}_i\mathrm{(E)}. \tag{5}$$

The major drawback of this approach in modelling TEY from realistic surfaces is the assumption that the sample is indeed in-depth uniform. Besides, we neglect emission of the second generation of electrons, emitted due to impingement of the emitted electrons hitting the surface protrusions.

3. Results and discussion

3.1. Thin film characterization

We considered in this work four different samples, summarized in Table 1 together with their surface morphology parameters:

- Sample 1 is the corrugated a-Si:H layer (rough);
- Sample 2 is the smooth a:Si-H layer (flat);
- Sample 3 is the corrugated a:Si-H layer coated by Al_2O_3 (rough AlOx);
- Sample 4 is the smooth Al_2O_3 layer (flat AlOx).

Table 1: Thickness d and surface roughness S_a of all samples from Ellipsometry, including the surface roughness S_a of the underlying substrate or layer.

	top layer			substrate/lower layer	
sample	material	d [nm]	S_a [nm]	material	S_a nm
1 rough	PECVD a-Si:H	17	10	polished c-Si	< 1
2 flat	PECVD a-Si:H	12	< 2	polished c-Si	< 1
3 rough AlOx	ALD Al_2O_3	5	10*	PECVD a-Si:H	10
4 flat AlOx	ALD Al_2O_3	5	< 1*	polished c-Si	< 1

*Roughness given by the underlying substrate or layer

The typical surface topography of the samples fabricated with different roughness is shown in figure 2 and 3. Both figures show a $2\times2\,\mu m^2$ AFM scan of a sample with $5\times5\,cm^2$ overall surface area. AFM measurements were done with a Bruker AFM Dimension Edge with the AFM probe TESPA-V2, which has a nominal tip radius of 7 nm. The topography was measured in tapping mode and image analysis was done with Gwyddion (Nečas and Klapetek (2012)). All surface parameters were calculated according to ISO standards.

For the corrugated a-Si:H layer in figure 2, we measured an average roughness of $S_a = 1.8\,nm$, with a mesokurtic shaped surface with normal peaks and a kurtosis of $S_{ku} = 3.01$. The latter indicates height distribution close to a perfect Gaussian.

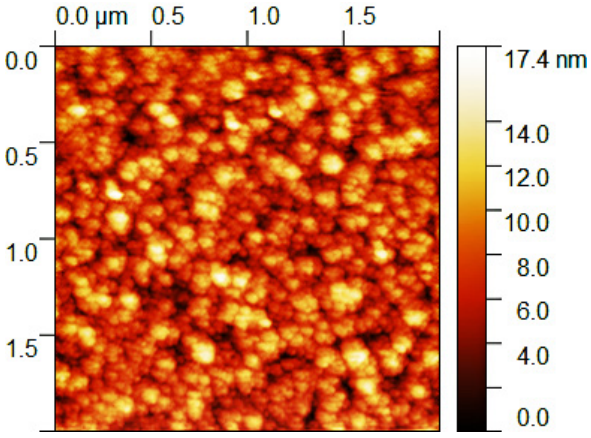

Mean roughness (Sa)	1.8 nm
Skew (Ssk)	-0.32
Excess kurtosis	0.17
Maximum height (Sz)	17.4 nm

Figure 2: AFM scan of the rough a-Si:H sample and resulting surface parameters.

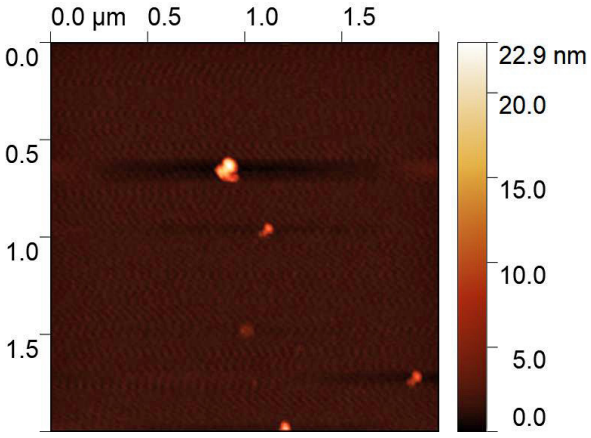

Mean roughness (Sa)	0.3 nm
Skew (Ssk)	12.6
Excess kurtosis	240
Maximum height (Sz)	22.9 nm

Figure 3: AFM scan of the flat a-Si:H sample and resulting surface parameters.

For the smooth a-Si:H layer shown in figure 3, we measured an average roughness of $S_a = 0.3\,\text{nm}$ and a kurtosis of $S_{ku} = 239.88$. The high kurtosis value indicates rather steep and rare peaks.

Considering that ALD coatings are highly conformal, figure 2 and 3 illustrate the typical surface texture of the corrugated and smooth AlOx samples as well.

Since the surface composition controls the secondary emission, we used XPS to analyse the chemical composition of the samples as deposited. The samples were inevitably exposed to air to perform the post-fabrication analysis. Samples would need to be plasma cleaned inside the measurement setup in order to determine the secondary yield of the pure material a-Si:H. As AMCPs are not plasma cleaned before use, we measured the samples as deposited in order to determine a most comparable data set. An overview of their surface composition is given in Figure 4. Carbon is a standard surface contaminant present in all samples, typically in the form of adventitious carbon (saturated aliphatic hydrocarbons). We see that its relative amount is increased for both AlOx samples, being the result of the ALD coating process. Small quantities of fluorine in the same samples most probably have the same origin. No XPS analysis of the smooth sample was performed as it was expected to behave as the corrugated sample. Hydrogen content is not detected by XPS, both a-Si:H layers (corrugated and smooth) are typically composed of about 10% hydrogen.

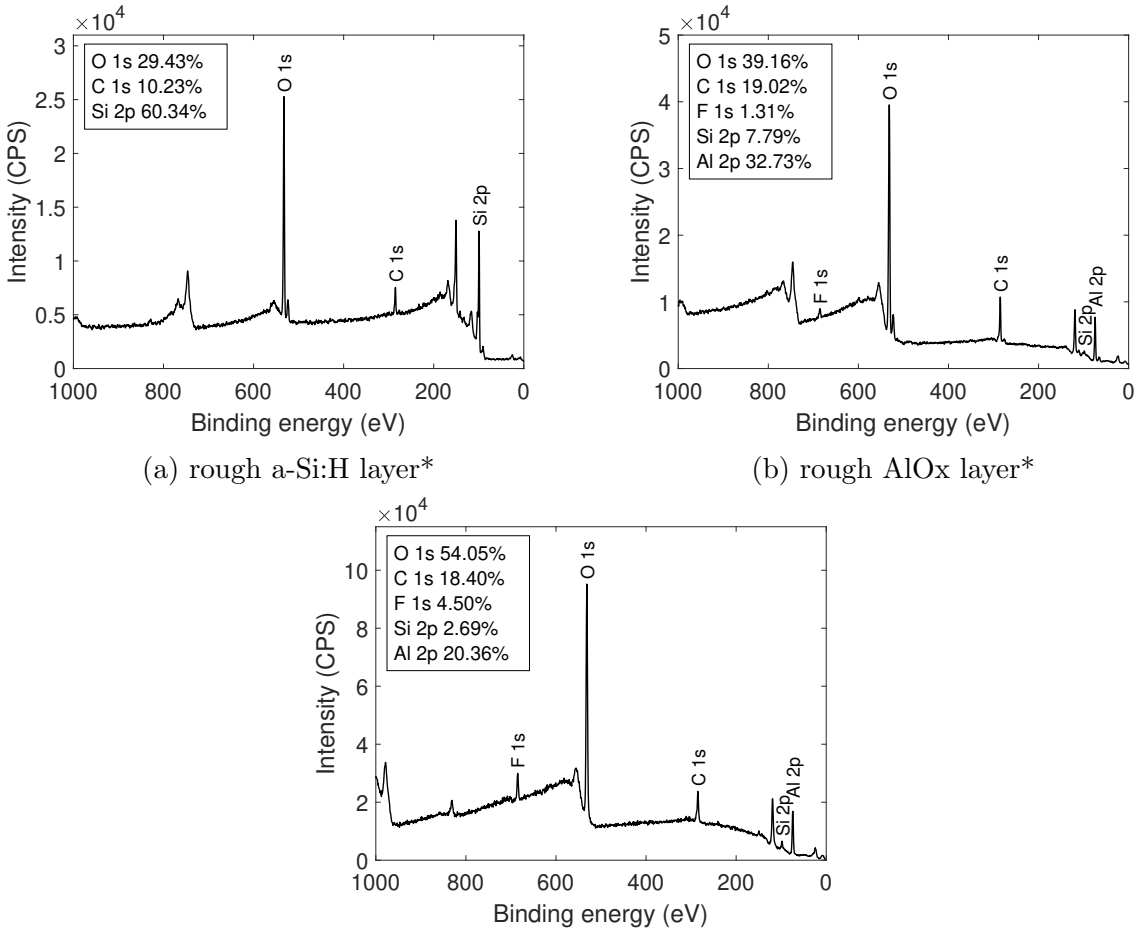

(a) rough a-Si:H layer*

(b) rough AlOx layer*

(c) flat AlOx layer

Figure 4: XPS spectra and resulting surface composition (atomic percent) of the corrugated a-Si:H layer and the corrugated and flat AlOx layer. *in situ XPS measurement

3.2. Emission yield

The TEY was measured for all samples at incident electron angles ranging from 0° (normal incidence) to 75° and for incident electron energies starting at 10 eV up to 1000 eV. Furthermore, the number of secondary electrons per incident electron, the secondary emission yield (SEY) was modeled for the AMCP surface.

3.2.1. Hydrogenated amorphous silicon The TEY of a-Si:H, measured for the corrugated and the smooth sample, is shown in figure 5. It was compared to experimental values of crystalline Si by Pierron et al. (2017); Bronshtein and Fraiman (1969) and from MC calculations by Pierron et al. (2017) and Kuhr and Fitting (1999). We also show the TEY of Si calculated with Nebula.

The measurements and simulations agree generally well for crystalline silicon, except for the low energy region where the more recent measurements by Pierron et al.

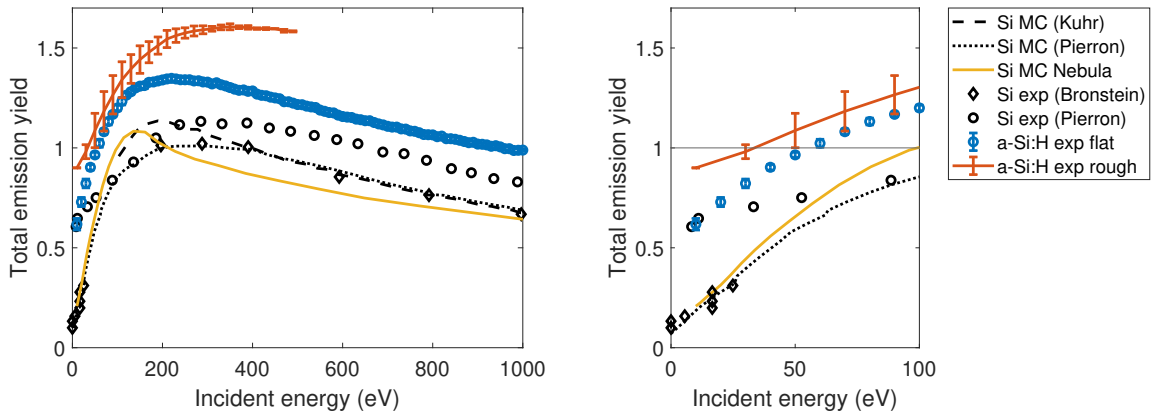

Figure 5: Total emission yield of a-Si:H measured for the smooth a:Si-H layer (flat) and the corrugated surface (rough) compared to literature values and simulations of crystalline Si.

(2017) show a higher yield than that predicted by the simulations. Of particular interest are the electron energies at which TEY = 1 (known as crossover energy), since the condition TEY > 1 is necessary to secure electron multiplication in MCPs. Compared to crystalline silicon, a-Si:H shows a higher emission yield and practically two times lower crossover energy of about 50 eV.

The incorporation of H into the atomic network of Si, yielding formation of a-Si:H, leads to H and OH termination. The overall effect is an increased electron emission yield of a-Si:H as compared to Si. This characteristic increase of the TEY due to H termination has also been observed for diamond by Shih et al. (1997). Indeed, electronic ab-initio calculations by Tao et al. (2015) have shown a decreased electron affinity of SiN through hydrogen termination, which effectively lowers the potential barrier for electron emission. The increase in emission yield observed here could thus be due to a lower potential barrier at the surface of a-Si:H. If this is not the case, the main reason for the increased TEY would be an increased energy gap, which forbids various energy loss processes and consequently extends the electron trajectories. The surface morphology of a-Si:H is also beneficial for secondary electron emission. With a maximum total emission yield over 1.6, the rough surface texture leads to a higher yield than the smooth surface. Additionally, we observe a further shift in the crossover energy of about 20 eV towards a lower energy for the corrugated a-Si:H sample compared to the smooth a-Si:H sample.

The TEY dependence on the incident angle is shown in figure 6. For higher incident angles we observe an increase towards higher yields. This is a well known phenomenon related with the deposition of the energy of primary electrons in a shallower region than at normal incidence. Therefore, the generated secondary electrons can be emitted with higher probability. This can be modeled for a number of pure conductive materials according to different approaches, such as the one presented by Bundaleski et al. (2015). It was demonstrated in the latter that the crossover energy shifts towards lower energies

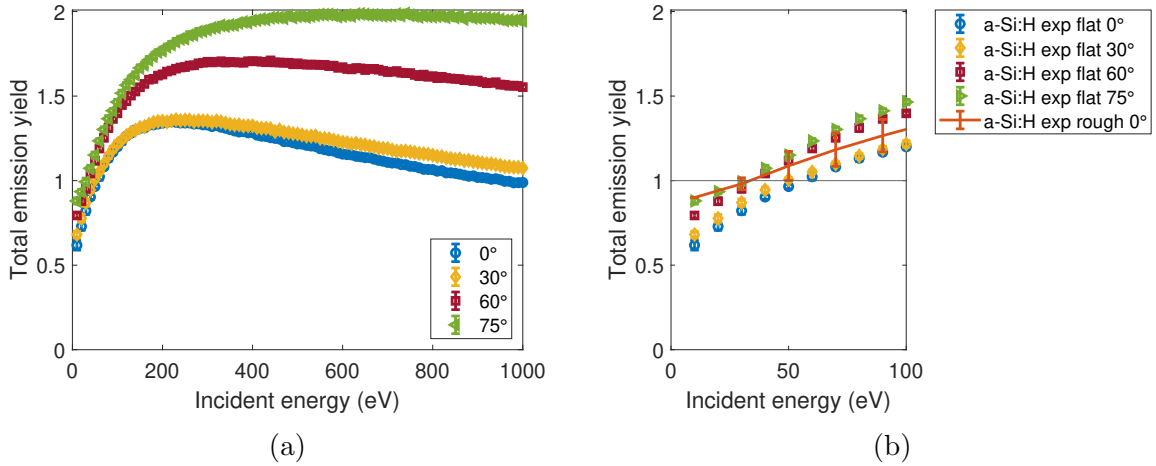

(a) (b)

Figure 6: (a) Total emission yield of a smooth a-Si:H sample, measured at incident angles of 0°, 30°, 60° and 75°, starting at 10 eV. (b) A zoom shows the crossover energy of a-Si:H with different surface textures (corrugated and smooth samples) and angles.

with increasing incident angle. In figure 6, we compare the crossover energy of the smooth layer at 75° with the measurements and literature values already shown in figure 5. The crossover energy for the smooth layer at 75° is about 20 eV lower than that at normal incidence. A decreased crossover energy is observed for the corrugated surface even at normal incidence. Indeed, this is due to local surface inclinations of corrugated surfaces, which cause an oblique incidence of primary electrons. This frequently results in amplification of the secondary electron emission. Due to the increase in elastic scattering for even higher incident angles, Bundaleski et al. (2015) predict a maximum yield at about 70°. Therefore, the TEY should decrease with further increasing angle.

In AMCPs an average emission yield of about 1.6 at an average incident energy of about 70 eV has been inferred from gain measurements of AMCP devices by Franco et al. (2014). Given the rough surface texture inside AMCP channels, this assumption is in good agreement with the observed trends. Electrons are accelerated with grazing trajectories in AMCPs and local electric field gradients could be the reason for an even further increase of their electron emission yield.

3.2.2. Aluminum Oxide While the inherent TEY of a-Si:H layers can be enhanced by roughening its surface, highly emissive layers need to be used to further improve AMCP performances. Hence the use of materials that can be deposited via ALD, since it is the only method capable of uniformly coating the inside of a channel with high aspect ratio. We show the total emission yield of Al_2O_3 in figure 7, where the measurements and MC calculations are compared to literature values.

Calculated TEY include results of MC simulations by Ivanov et al. (2018) at the respective incident angles of 0° and 80°. van der Graaf et al. (2017) used a low energy MC extension of a GEANT4 code to obtain the curves presented here. Additionally to

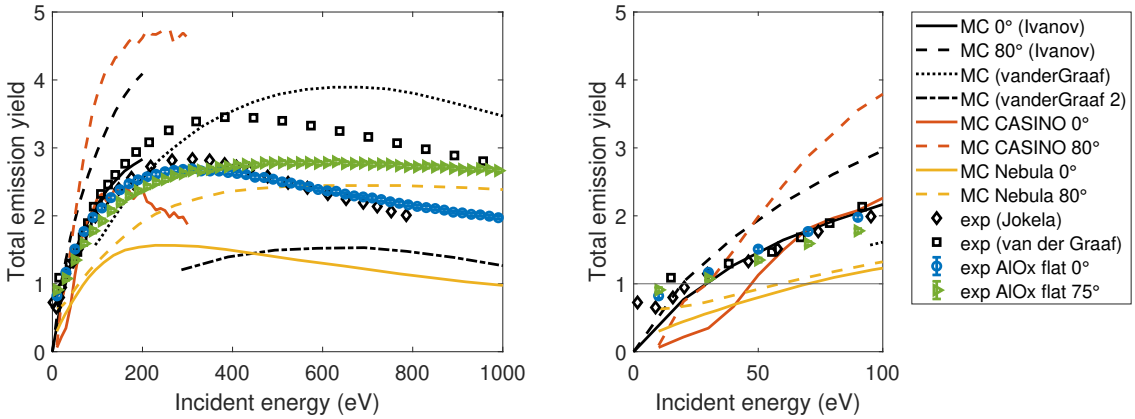

Figure 7: Al_2O_3 total emission yield measurements and simulations compared to experimental and calculated literature values.

results from Nebula, we show results from Casino. The total emission yield of Al_2O_3 has been measured experimentally by Jokela et al. (2012) for a 4 nm thick layer and by van der Graaf et al. (2017) for a 12.5 nm thick one. In figure 7, we show the experimental total emission yield of Al_2O_3 at 0° incidence and at 75° incidence.

It can be observed that the different assumptions in the theoretical models lead to a great variation of the resulting TEY. The experimental emission yield data on the other hand agree well, especially in the low energy range. A higher maximum yield of the experimental result by van der Graaf et al. (2017) could be due to the layer thickness. Thicker layers of Al_2O_3 are expected, theoretically, to exhibit a higher yield, when charging is avoided. As seen in the previous section, higher incident angles on flat layers also increase TEY. In reality the surface morphology, surface contamination and charging effects greatly affect experimental results. The TEY of the smooth of Al_2O_3 layer at 75° is below the expected increase with incident angle. This and the flattened shape of the curve indicate that this particular measurement was subject to charging.

The increase of the TEY on a corrugated a-Si:H layer by using a highly emissive Al_2O_3 coating is shown in figure 8. As the highly resistive a-Si:H layer leads to charging of the surface, the secondary yield of Al_2O_3 cannot be fully determined when deposited on this rough surface. However, despite this charging effect and a total layer thickness of about 22 nm, we observe a higher secondary electron yield with the additional Al_2O_3 coating compared to the yield of the 17 nm thick corrugated a-Si:H layer.

Typically, the ALD deposition temperature of Al_2O_3 is between 200°C and 300° (Guo et al. (2019)). We found that the deposition temperature has no significant effect on the TEY, as shown in figure 8. The smooth Al_2O_3 layer, prepared at 200°C and a similar layer deposited at 300°C with otherwise identical parameters exhibit almost identical TEY values.

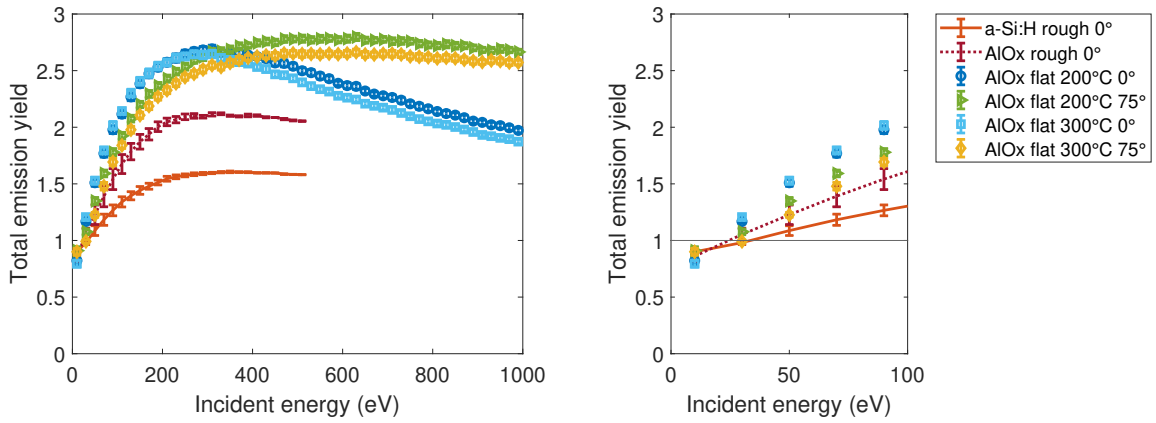

Figure 8: The total emission yield of Al_2O_3 (flat AlOx) fabricated at temperatures of 200°C and 300°C respectively, was measured at incident angles of 0° and 75°. The total emission yield of the corrugated a-Si:H layer is improved by an Al_2O_3 coating (rough AlOx), even though limited by charging when compared to the total emission yield of the smooth Al_2O_3 layer.

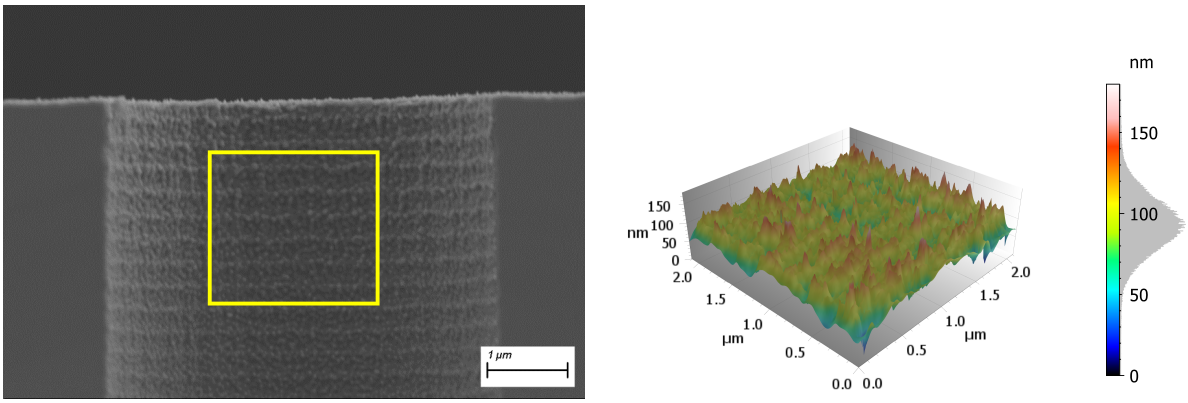

(a) (b)

Figure 9: (a) SEM image showing the surface morphology inside an AMCP channel. (b) Height profile z(x,y) and height distribution of the AMCP channel for the area marked in (a).

3.3. Total emission yield in AMCPs

How do the previous results allow one to deduce the TEY in AMCPs? As previously seen, the total emission yield largely depends on the surface morphology. Therefore, we considered the influence of the real surface structure in AMCP channels, shown in figure 9. In general, the surface inside the channel varies depending on the fabrication process and within one channel, along its depth. We also discuss the TEY for the limit of electrons with negligible energy approaching 0 eV.

3.3.1. Modelling TEY of the AMCP channel surface Using the measured TEY(E) of smooth and corrugated a-Si:H layers shown in section 3.2.1, the expected emission yield of a corrugated AMCP channel surface has been calculated based on the model described in section 2.4. The aim of this calculation was to evaluate the possible effects of the AMCP channel surface morphology on the TEY.

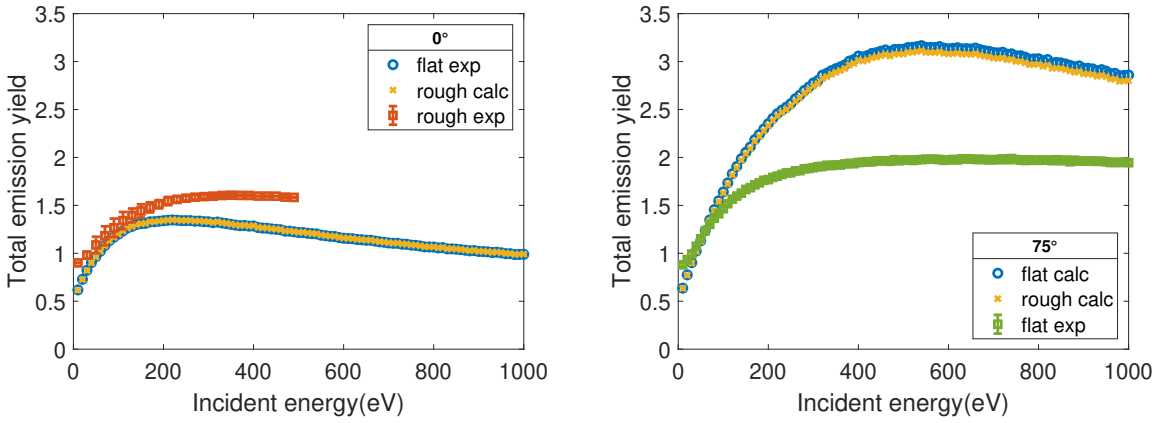

(a) (b)

Figure 10: (a) TEY of the corrugated a-Si:H surface shown in figure 2 was calculated (rough calc) using TEY of the flat a-Si:H layer (flat exp) as a calibration and compared to the measurement (rough exp) at 0°. (b) TEY for the rough and the flat layer were calculated at 75° and compared to the experimental TEY of the flat layer.

As a first step, the expected emission yields of the smooth and corrugated a-Si:H layers were calculated from their surface scans smooth sample at 0° was taken from the experiment to calibrate the TEY(E) model. Hence, the calculated TEY at 0° (flat calc) corresponds to the measured TEY (flat), as shown in figure 10 a. The calculated TEY for the corrugated surface (rough calc) shows a similar yield. In figure 10 b, we show the calculated TEY at 75° for the smooth (flat calc) and corrugated surface (rough calc) and the experimental TEY for the smooth sample (flat). The difference in surface roughness does not lead to a significant difference in TEY according to the calculations. The experimental yield however is significantly different from the calculated ones. Since the experimental TEY cannot be explained by the surface roughness, other effects, like hydro-carbonation of the surface or, charging effects might have caused a lower experimental yield than expected for the corrugated surface as well.

The surface corrugation function z(x,y) of the AMCP channel was reconstructed from an SEM image and is shown in figure 9. The expected TEY of this surface morphology was calculated (channel) and is shown in figure 11 alongside the calculated yield for the smooth surface (flat).

From the theoretical electron emission model, the surface morphology of the channel is expected to reduce the TEY, as electrons can be recaptured. In an operating AMCP on the other hand, the local electric field strength varies and could lead to re-emission

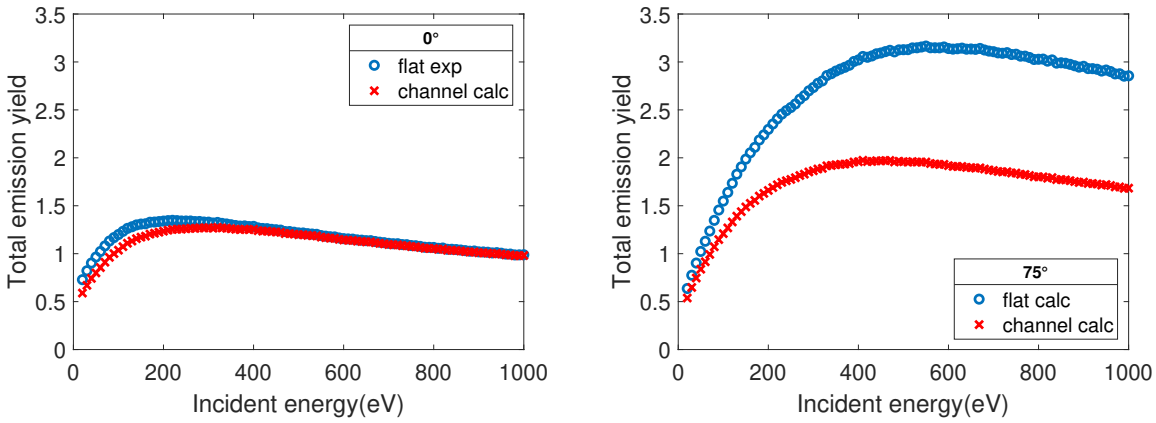

(a) (b)

Figure 11: (a) TEY of the AMCP channel surface shown in figure 9 was calculated (channel calc) at 0°. The TEY of a perfectly smooth a-Si:H layer (flat exp) at 0° served as a calibration. (b) The calculated TEY for the flat sample and for the channel surface are shown at 75°.

of electrons and a lowered crossover energy. This means that, in general, surface morphology alone cannot be used to calculate secondary yield in AMCP channels, and while TEY measurements of a-Si:H layers can be used as a basis, the secondary yield of AMCPs must be deduced from AMCP gain measurements. Moreover, the maximum yield, and the yield curve at higher energies as just presented determine only a fraction of the electron dynamics, whereas the crossover energy plays a major role in determining the level of multiplication in the channel. The expected lowering of the crossover energy for corrugated surfaces could not be observed with the model.

3.3.2. Discussion - Total emission yield at low energies Overall, we found in the previous section that the total emission yield decreases below 1 only for energies below 40 eV. Notably, the measured TEY does not approach 0 when the incident energy approaches 0 eV. In fact, elastic scattering is the predominant process at low energies, as will be confirmed in the following section. However, the TEY for incident electrons with energies close to 0 eV might be prone to the following measurement artefacts. Electrons may not reach the surface and therefore not interact with the surface at all. Also, electrons may be absorbed. The nature of the interaction and the resulting TEY depend as well on the local work function, which is not uniform for the samples presented here. Furthermore, the electron beams used to measure TEY consist of electrons with an energy spread of about 0.8 eV. In theory, it can be assumed that TEY(0 eV)=1 as discussed by Cazaux (2012), which has been shown experimentally for selected materials by Cimino et al. (2015). For AMCP modelling we assume hence a TEY(0 eV)=1, where all electrons are backscattered, when absorption and other effects are neglected.

With the previous results, we provided an overview of the magnitude and slope of

the TEY at low energies as well as the crossover energies of a-Si:H and Al_2O_3 and their dependencies on surface corrugation and incoming angle. Due to the influence of the surface chemistry and texture on the emission yield, the AMCP channel surface cannot be fully represented as a thin film and thus cannot be fully characterized by electron emission measurements. However, the present study is a valuable starting point for the parametrization of emission yield curves in order to describe the multiplication process, in the low energy regime, in electron multipliers.

3.4. Emission energy

The goal of this analysis is to describe the operation of an AMCP channel, where we are studying an electron 'cascade': the energy of each emitted electron has a direct consequence on its incident energy and angle, which then affects the number of electrons emitted and trajectories in the forthcoming steps. As presented above, the number of emitted electrons depends on the incident electron energy. At a fixed electric potential and AMCP channel geometry, and assuming a cosine function for the emission angle of electrons, the incident energy and angle of an electron i.e. the TEY and therefore the number of electrons in the cascade solely depends on the electron emission energy.

The emission energy distribution $N(E_e)$ was measured for incident energies below 200 eV for the rough a-Si:H layer and the rough Al_2O_3 layer. The emission energy distribution was determined with the electron energy analyzer shown in figure 1b for the effective incident electron energies of 12.5 eV-192.5 eV for a-Si:H and 3.5 eV-194.5 eV for Al_2O_3, corrected according to the equation 2 and according to their work function taken from Cazaux (2010). The spectra are shown in figure 12.

Emitted electrons can be categorized according to the physical process they undergo when interacting with the surface: secondary electrons (SE), inelastically backscattered electrons (IBS) and elastically backscattered electrons (EBS). Because SE and IBS can not be separated at low energies and for the purpose of comparing the measurements with literature values, we artificially divide the spectrum into three parts, although this does not have a physical meaning. EBS are characterized by an emission energy close to the incident energy (+/- 2 eV). An emission energy both below 50 eV and 2 eV below the incident energy refers to a SE. The other electrons are considered as IBS. For primary electron energies below 50 eV we consider all electrons which are not EBS as secondary.

The TEY presented in section 3.2 is the sum of the secondary emission yield δ, the EBS yield η_e and IBS yield η_{ie}. Several empirical (Vaughan (1989)) and semi-empirical models (Bundaleski et al. (2015)) exist that describe δ. Therefore the resulting secondary yield curve can also be parameterized. The backscattering yield can also be described by existing models by Cazaux (2012); Cimino et al. (2004); Jablonski (2014). We used this categorization to obtain, with the help of the emission spectra measured at few energies shown above 12, probability functions for electron emission energies for all incident electron energies up to 500 eV. These functions could then be used for AMCP simulations.

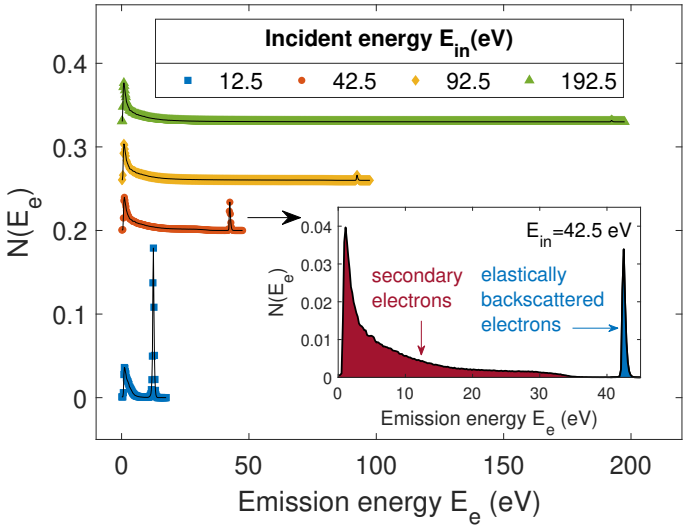

(a) a-Si:H

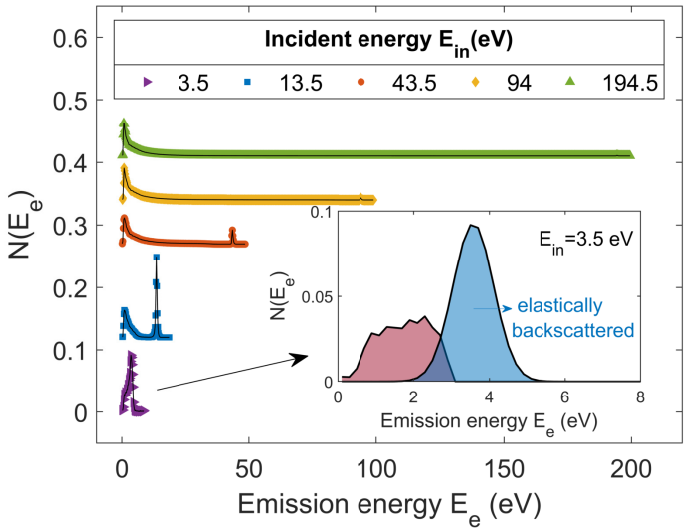

(b) Al_2O_3

Figure 12: (a) Corrected a-Si:H emission spectra for incident energies of 12.5 eV, 42.5 eV, 92.5 eV and 192.5 eV. The inset shows the emission spectrum for 42.5 eV. We can identify the elastic peak at 42.5 eV, secondary electrons are all electron emitted with lower energies. (b) Corrected Al_2O_3 emission spectra for incident energies of 3.5 eV, 13.5 eV, 43.5 eV, 94 eV, 194.5 eV. The inset shows the emission spectrum for 3.5 eV, where the elastic peak overlaps with emission of electrons with less than the incident energy.

3.4.1. Relative backscattering probability At first, we used the energy spectra shown above to deduce the relative backscattering probability P. P is a useful measure to determine the relative proportion of high energy electrons versus low energy electrons that are emitted upon an incident electron with a particular energy. P is particularly useful in the event of elastic scattering, as all elastically backscattered electrons are emitted with the same as the incoming energy and their total emission yield is 1. The elastic and inelastic backscattering yields are related to P in the following way: $\eta_{e/ie} = P_{EBS/IBS} \cdot TEY$. We calculated P_{EBS} as the integral of the elastic peak divided by the integral of the whole emission function. Figure 12 a) shows an inlet for 42.5 eV, where the area of the elastic peak is colored in blue, whereas the area of the secondary electron distribution function is colored in red. Similarly, P_{IBS} is calculated from the integral of the remaining energies between 50 eV and the elastic peak.

As shown in the spectra in figure 12, we measured $P_{EBS/IBS}$ in four points for a-Si:H and in five points for Al_2O_3. In order to determine the backscattering probabilities for every possible incident energy in AMCPs, the experimental data points were fitted with an exponential decay function for the elastic contribution P_{EBS} and with a linear function for the inelastic contribution P_{IBS}. The probability of elastic backscattering at 0 eV was set to 1 $P_{EBS}(0) = 1$ as in Cazaux (2012). The functions $P_{EBS/IBS}$ were arbitrary ones chosen to describe the experimental behavior:

$$P_{EBS}(E_{in}) = (1-a)\exp\left(-b \cdot E_{in}\right) + a \text{ for } E_{in} < 50 \text{ eV} \tag{6}$$

$$P_{EBS+IBS}(E_{in}) = P_{EBS}(E_{in}) + c \cdot E_{in} + d \text{ for } E_{in} \geq 50 \text{ eV}. \tag{7}$$

The fit values are given in table 2.

Table 2: Fit values for the backscattering probability according to equations 6 and 7.

	a	b	c	d
a-Si:H	0.01	0.05	$4{\cdot}10^{-5}$	0.05
Al_2O_3	0.005	0.06	$2{\cdot}10^{-5}$	0.03

We compared the incident electron energy dependence of the backscattering probability measured here for a-Si:H with existing literature values of Si, and with the results of MC calculations using Nebula and CASINO in figure 13. A similar comparison is shown for Al_2O_3 in figure 14. An additional dependence of the backscattering probability on the incident angle can be observed for both materials, which was not taken into account in the parametrization. For both materials, variations in the relative backscattering are important in the low energy range below 50 eV. Consequently, the parametrization presented in this section can be used to separate the total emission yield into its respective contributions and calculate electron emission energies in AMCPs.

3.4.2. Secondary emission energy distribution As secondary electrons drive AMCP performance, quantifying their emission energies is crucial for an understanding of the

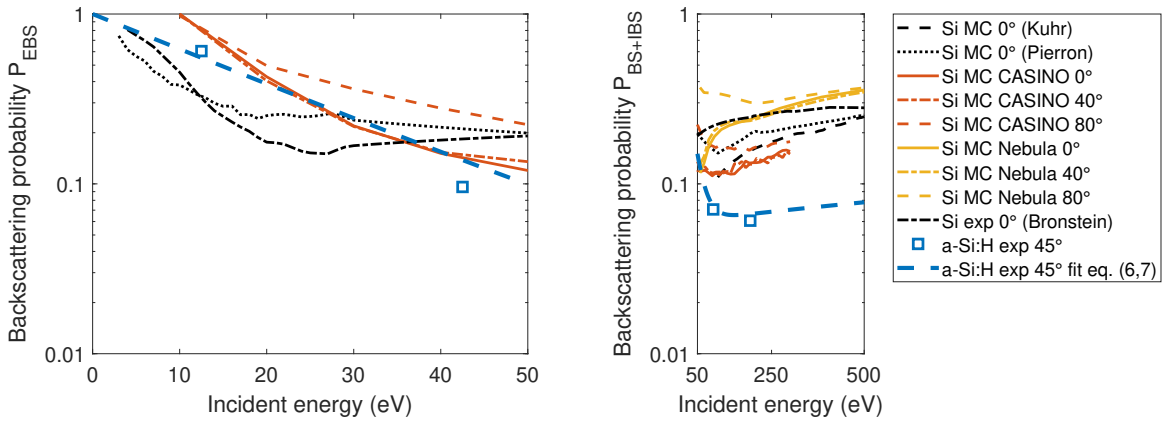

Figure 13: Experimental a-Si:H backscattering probability at 45°, measured at four points (see figure 12) and fitted with equations 6 and 7, compared to MC simulations, simulated and experimental literature values.

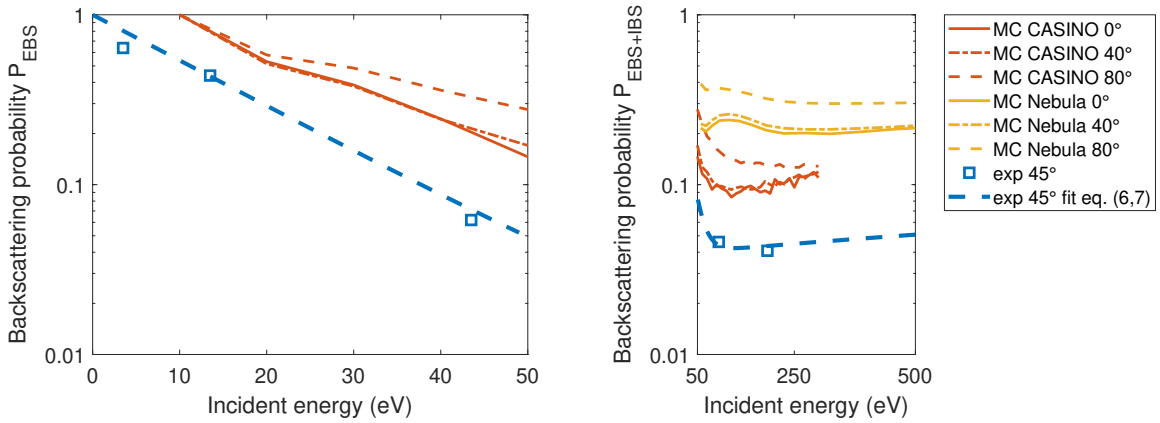

Figure 14: Experimental backscattering probability of Al_2O_3 measured at five points (see figure 12) and fitted with equations 6 and 7, compared to the simulation results and values found in the literature.

avalanche process in an AMCP channel. In this section, we compare the low energy part of the a-Si:H emission energy spectrum to theoretical and experimentally measured secondary electron energy E_s distributions $\partial\delta/\partial E_s(E_{in})$ of a-Si:H and c-Si in figure 15. While secondary electrons are commonly defined to have an energy cutoff at 50 eV, most of the secondary electrons are emitted with energies below 10 eV.

The analytical functions include a physics based model by Henke et al. (1979) with

$$d\delta/dE_s(E_s,\chi,E_g) = C \cdot \frac{E_s}{(E_s+\chi-E_g)^2 \cdot (E_s+\chi)^{5/2}} \tag{8a}$$

for semiconductors and

$$d\delta/dE_s(E_s,\chi) = C \cdot \frac{E_s}{(E_s+\chi)^3} \tag{8b}$$

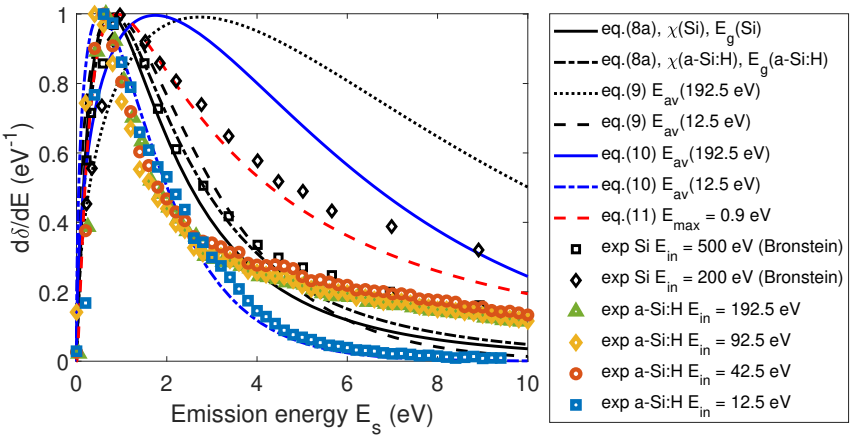

Figure 15: Measured secondary emission energy distribution compared to theoretical curves from literature for a-Si:H and Si.

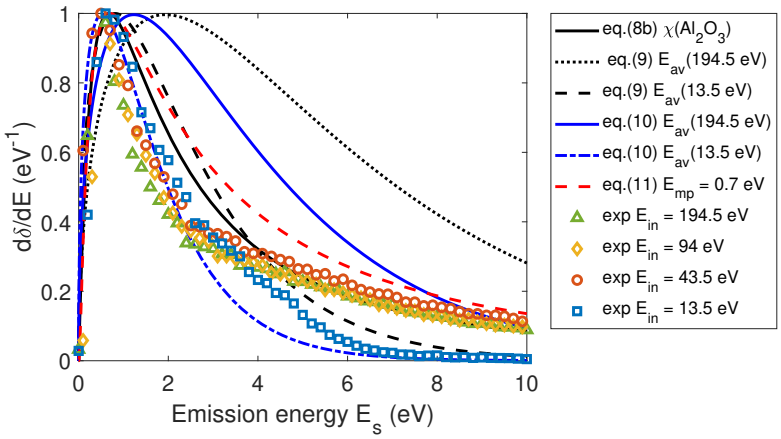

Figure 16: Secondary emission energy distribution compared to theoretical curves from literature for Al_2O_3.

for insulators, where χ is the electron affinity, E_g the band gap and C a normalization constant. We use the values listed in table 3 for χ and E_g. The model is based upon the assumption that the electrons are ejected from the valence band. Empirical secondary

Table 3: Electron affinity and band gap of Si, a-Si:H and Al_2O_3.

	Si	a-Si:H	Al_2O_3
Electron affinity χ (eV)	3.2	3.92	1.35
Band gap E_g (eV)	1.12	1.8	7.0/7.6 Filatova and Konashuk (2015)

electron distribution functions are typically used for MCP modelling by Yakobson (1966); Price and Fraser (2001); Kruschwitz et al. (2011). All of these functions are phenomenological. The fit function by Yakobson (1966) is

$$d\delta/dE_s(E_s, E_{av}) = C \cdot E_{av}^{-1.5} \cdot \sqrt{E_s} \exp\left(-1.5\frac{E_s}{E_{av}}\right). \quad (9)$$

with the average emission energy E_{av}. We use $E_{av}(E_{in} = 12.5\,\text{eV}) = 2.5\,\text{eV}$ with a normalization factor of $C = 5$ and $E_{av}(E_{in} = 192.5\,\text{eV}) = 8.2\,\text{eV}$ with $C = 22.9$. Furthermore, we tested the fit function of Price and Fraser (2001)

$$d\delta/dE_s(E_s, E_{av}) = 3.3 \cdot (E_s/E_{av})^{0.47} \cdot \exp\left(-2.21 \cdot E_s/E_{av}\right) \quad (10)$$

and the fit function of Kruschwitz et al. (2011)

$$d\delta/dE_s(E_s, E_{mp}) = \exp\left(\frac{-(\log\left(E_s/E_{mp}\right))^2}{2 \cdot 1.33^2}\right) \quad (11)$$

with the most probable emission energy $E_{mp} = 0.9\,\text{eV}$. None of the theoretical curves can represent the measured curves perfectly, as shown in figure 15. We found the best fit with equations 11 and 8a for incident energies above 25 eV. Although the fit function of the equation 10 may be appropriate for the energy spectrum at $E_{in} = 12.5\,\text{eV}$, it does not hold for higher incident energies.

The low energy part of the Al_2O_3 spectra were compared to the theoretical secondary electron distribution curves of Al_2O_3 in figure 16. Here, the best fit was obtained with the theoretical curve of equation 8b for incident energies above 25 eV. None of the functions could be used to represent the energy spectrum at $E_{in} = 13.5\,\text{eV}$.

For incident energies below 25 eV, the emission energy distributions of both materials depend on the incident energy and cannot be represented by any of the functions above. In this energy range we use an energy dependent fit function for incident energies below 25 eV for a-Si:H and Al_2O_3 using an energy dependence proposed for copper and stainless steel by Furman and Pivi (2002):

$$\partial\delta/\partial E_s(E_{in}) = \frac{\Gamma((P_1 + P_2)/2) \cdot (P_1/P_2)^{P_1/P_2} \cdot E_s^{P_1/P_2 - 1}}{\Gamma(P_1/2) \cdot \Gamma(P_2/2) \cdot (1 + P_1/P_2 \cdot E_s)^{(P_1+P_2)/2}} \quad (12)$$

where $\Gamma(x)$ is the Gamma function of x and x is an integer. In contrast to the original interpretation of P_1 and P_2 as probabilities of emitting 1 or 2 electrons, respectively, we consider these magnitudes as functions of the incident energies. The best fit was obtained for $P_1 = 39 \cdot \exp(-E_{in}/68) + 111$ and $P_2 = 2$. The fit function is shown in figure 17, where the resulting probability density function (PDF) is compared with the measured secondary electron emission spectra of a-Si:H and Al_2O_3. In the same figure we also present corresponding cumulative distribution functions, obtained by integration of the PDFs, which are necessary for performing MC simulations of AMCPs.

From the energy distribution analysis in this chapter we derived a parameterization for the energy dependence of elastic backscattering. While secondary emission energy models from literature could represent the emission energy spectrum for high incident energies, we found that at low incident energies, the electron energy spectrum depends

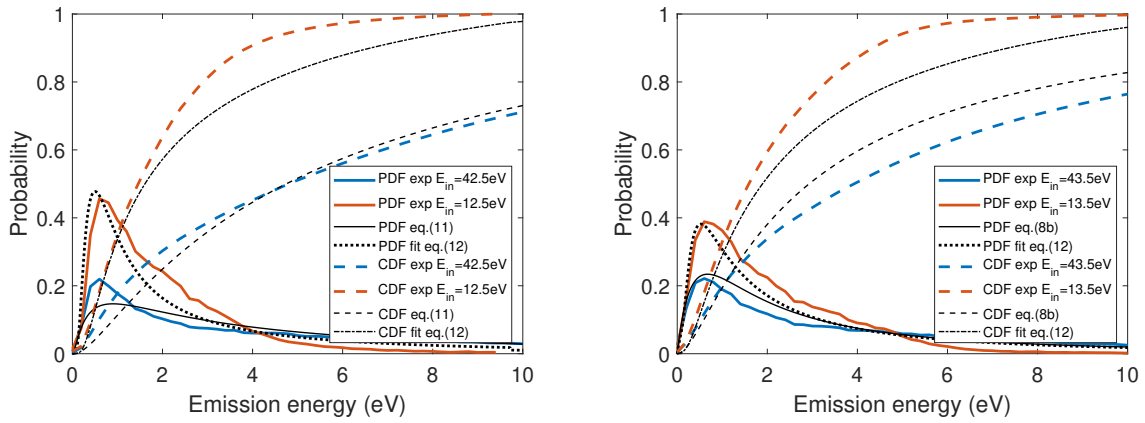

(a) a-Si:H (b) Al_2O_3

Figure 17: Probability density function (PDF) and cumulative distribution function (CDF) of the secondary electron emission energy for low primary electron energies E_{in} and their fit functions.

on the incident energy. Finally, we showed a suitable parameterization for the energy emission spectrum of both a-Si:H and Al_2O_3 using equation 12 at low incident energies.

4. Conclusion

In this paper, we provide a complete analysis of electron emission characteristics, which is necessary for reliable AMCP modelling. The electron emission energy distribution and the emission yield of a-Si:H and Al_2O_3 with two different surface textures have been characterized at low incident electron energies. A comparison to literature values confirmed the need for this detailed analysis, as there are significant variations between measurements, analytical expressions and Monte Carlo models. Furthermore, we defined parametrizations for the expected electron scattering process depending on the incident electron energy and determined analytical functions describing the energy dependence of the secondary electron energy distribution.

In general, amorphous silicon shows a higher emission yield than crystalline silicon which has a maximum yield below 1.2. The average emission yield of a-Si:H is about 1.6, deduced by Franco et al. (2014) from the operation of AMCPs. In the present study, a rough surface leads to a further increase of the electron emission yield of amorphous silicon up to a maximum of approximately 1.6 at normal and of 2 at 75 degree incidence. Curvature and trenches in a microchannel modify the actual surface texture in the channel and therefore influence the emission yield and the crossover energy such that it cannot be reconstructed based on thin film measurements. In addition, the local electric field strength in AMCP channels under operation can modify the secondary emission yield. Together with electron incidence at grazing angles, this could be the reason for the effective emission yield of 1.6 observed so far in AMCPs.

Since coatings with highly emissive ALD films are the key to improve the potentially high gain achievable with AMCPs, we explored the low energy electron emission properties of ALD-deposited Al_2O_3. We measured a maximum emission yield of up to 2.8. The TEY of Al_2O_3 can be further increased by increasing the film thickness. Yield values up to 3.5 were measured and theoretic models by van der Graaf et al. (2017) predict even higher electron yields.

We determined the energy and angular dependencies of the emission energy distribution for a-Si:H and Al_2O_3. In accordance with literature, the probability for elastic backscattering is high at low incident energies. For incident energies below 25 eV, the secondary emission spectrum depends on the incident energy, which is not the case for higher incident energies. For electron multiplication processes at these low energies, such as in AMCPs, this emission energy variation needs to be considered.

With the present analysis, the determining factors of electron emission at low energies in a-Si:H were identified and extended for Al_2O_3. The angular dependence and energy dependence of the electron emission yield and energy distribution are therefore understood and can be used for more detailed modelling and thus further development of electron multipliers. This can be particularly relevant for developing electron multipliers that deviate from the cylindrical shape of microchannels.

This study could also be extended to other highly emissive layers that can be deposited via ALD, such as MgO, Ti doped MgO or multi layered structures as indicated by Tao et al. (2016). With a maximum yield of more than 10 for an 11 nm layer measured by Jokela et al. (2011), MgO has a real potential to tremendously improve AMCP performance and could enable them to reach a multiplication factor well above 10^5.

5. Acknowledgements

We are grateful to Philippe Wyss for deposition of the flat a-Si:H layers, Mohammad Beygi for AFM imaging and Pierre Mettraux for the XPS analysis of the flat Al_2O_3 layer. Results presented here were obtained with the financial support of the Swiss National Science Foundation project 200021_162525/1, the Swiss National Science Foundation through the Sinergia program (Grant No. 177165, 2018–2022) and the Portuguese National Funding Agency for Science, Research and Technology in the framework of the project CERN/FIS-TEC/0039/2019 and the grants UIDB/00068/2020 and UIDP/00068/2020.
The authors have no conflicts of interest to declare.

References

Andronov A, Smirnov A, Kaganovich I, Startsev E, Raitses Y and Demidov V 2013 *AIP Conf. Proc. C* **1206051**, 161–163. 3 p. Comments: 3 pages, contribution to the Joint INFN-CERN-EuCARD-AccNet Workshop on Electron-Cloud Effects: ECLOUD'12; 5-9 Jun 2012, La Biodola, Isola d'Elba, Italy.
URL: *http://cds.cern.ch/record/1601946*

Balcon N, Payan D, Belhaj M, Tondu T and Inguimbert V 2012 *IEEE Transactions on Plasma Science* **40**(2 PART 1), 282–290.

Belhaj M, Tondu T, Inguimbert V, Barroy P, Silva F and Gicquel A 2010 *Journal of Physics D: Applied Physics* **43**(13).

Blayo N and Drévillon B 1992 *Surface Science* **260**(1), 37–43.
URL: *https://www.sciencedirect.com/science/article/pii/003960289290016Y*

Bronshtein I M and Fraiman B S 1969.

Bundaleski N, Belhaj M, Gineste T and Teodoro O M 2015 *Vacuum* **122**, 255–259.
URL: *http://dx.doi.org/10.1016/j.vacuum.2015.04.010*

Cauchy L 1830 *bull. des. sc. maht.* **14**, 9.

Cazaux J 2010 *Ultramicroscopy* **110**(3), 242–253.
URL: *http://dx.doi.org/10.1016/j.ultramic.2009.12.002*

Cazaux J 2012 *Journal of Applied Physics* **111**(6), 064903.
URL: *http://aip.scitation.org/doi/10.1063/1.3691956*

Cimino R, Collins I R, Furman M A, Pivi M, Ruggiero F, Rumolo G and Zimmermann F 2004 *Physical Review Letters* **93**(1), 014801–1.

Cimino R, Gonzalez L A, Larciprete R, Di Gaspare A, Iadarola G and Rumolo G 2015 *Phys. Rev. ST Accel. Beams* **18**, 051002.
URL: *https://link.aps.org/doi/10.1103/PhysRevSTAB.18.051002*

Demers H, Poirier-Demers N, Couture A R, Joly D, Guilmain M, de Jonge N and Drouin D 2011 *Scanning* **33**(3), 135–146.
URL: *http://doi.wiley.com/10.1002/sca.20262*

Elam J W, Xiong G, Han C Y, Wang H H, Birrell J P, Welp U, Hryn J N, Pellin M J, Baumann T F, Poco J F and Satcher J H 2006 *Journal of Nanomaterials* **2006**, 1–5.

Filatova E O and Konashuk A S 2015 *The Journal of Physical Chemistry C* **119**(35), 20755–20761. Publisher: American Chemical Society.
URL: *https://doi.org/10.1021/acs.jpcc.5b06843*

Fitting H J, Schreiber E, Kuhr J C and von Czarnowski A 2001 *Journal of Electron Spectroscopy and Related Phenomena* **119**(1), 35–47.
URL: *https://doi.org/10.1016/S0368-2048(01)00232-8 https://linkinghub.elsevier.com/retrieve/pii/S0368204801002328*

Franco A 2014.
URL: *http://infoscience.epfl.ch/record/200863*

Franco A, Geissbühler J, Wyrsch N and Ballif C 2014 *Scientific Reports* **4**(August 2015), 1–7.
URL: *http://www.nature.com/doifinder/10.1038/srep04597*

Frey S, Loffler J, Ballif C and Wyrsch N 2019 *in* '2019 IEEE Nuclear Science Symposium and Medical Imaging Conference, NSS/MIC 2019' Institute of Electrical and Electronics Engineers Inc.

Furman M A and Pivi M T 2002 *Physical Review Special Topics - Accelerators and Beams* **5**(12), 82–99.

Guo J, Wang D, Xu Y, Zhu X, Wen K, Miao G, Cao W, Si J, Lu M and Guo H 2019 *AIP Advances* **9**(9), 095303.
URL: *https://doi.org/10.1063/1.5113671*

Henke B L, Liesegang J and Smith S D 1979 *Physical Review B* **19**(6), 3004–3021.

Ivanov V, Barnyakov A and Barnyakov M 2018 *Nuclear Instruments and Methods in Physics Research, Section A: Accelerators, Spectrometers, Detectors and Associated Equipment* **903**(June), 170–174.
URL: *https://doi.org/10.1016/j.nima.2018.05.046*

Jablonski A 2014 *Journal of Physics D: Applied Physics* **47**(5).

Jokela S J, Veryovkin I V, Zinovev A V, Elam J W, Mane A U, Peng Q and Insepov Z 2012 *Physics Procedia* **37**, 740–747.
URL: *http://linkinghub.elsevier.com/retrieve/pii/S1875389212017567*

Jokela S J, Veryovkin I V, Zinovev A V, Elam J W, Peng Q and Mane A U 2011 *AIP Conference Proceedings* **1336**, 208–212.

Joy D and Luo S 1989 *Scanning* **11**(4), 176–180.

Kieft E and Bosch E 2008 *Journal of Physics D: Applied Physics* **41**(21).

Kruschwitz C A, Wu M and Rochau G A 2011 *Review of Scientific Instruments* **82**(2).

Kuhr J C and Fitting H J 1999 *Journal of Electron Spectroscopy and Related Phenomena* **105**(2-3), 257–273.

Ladislas Wiza J 1979 *Nuclear Instruments and Methods* **162**(1-3), 587–601.
URL: *http://linkinghub.elsevier.com/retrieve/pii/0029554X79907341*

Löffler J, Thomet J, Belhaj M, Kessel L V, Hagen C W, Ballif C and Wyrsch N 2019 *IEEE Nucl. Sci. Symp. Conf. Rec.* pp. 1–6.
URL: *https://ieeexplore.ieee.org/document/9059971*

Löffler J, Ballif C and Wyrsch N 2018 *Nuclear Instruments and Methods in Physics Research Section A: Accelerators, Spectrometers, Detectors and Associated Equipment* **912**, 343–346.
URL: *https://linkinghub.elsevier.com/retrieve/pii/S0168900217314262*

Nečas D and Klapetek P 2012 *Central European Journal of Physics* **10**, 181–188.

Pierron J, Inguimbert C, Belhaj M, Gineste T, Puech J and Raine M 2017 *Journal of Applied Physics* **121**(21).
URL: *https://doi.org/10.1063/1.4984761*

Price G J and Fraser G W 2001 *Nuclear Instruments and Methods in Physics Research, Section A: Accelerators, Spectrometers, Detectors and Associated Equipment* **474**(2), 188–196.

Salvat F, Jablonski A and Powell C J 2005 *Computer physics communications* **165**(2), 157–190.

Schulte S, Hartung G, Kröger J, Himmerlich M, Petit V and Taborelli M 2020 *Physical Review Accelerators and Beams* **23**(10), 103101.
URL: *https://doi.org/10.1103/PhysRevAccelBeams.23.103101*

Shih A, Yater J, Hor C and Abrams R 1997 *Applied Surface Science* **111**, 251–258.

Tao S X, Chan H W and Van der Graaf H 2016 *Materials* **9**(12).
URL: *https://www.mdpi.com/1996-1944/9/12/1017*

Tao S X, Theulings A, Smedley J and Van Der Graaf H 2015 *Diamond and Related Materials* **53**, 52–57.

van der Graaf H, Akhtar H, Budko N, Chan H W, Hagen C W, Hansson C C, Nützel G, Pinto S D, Prodanović V, Raftari B, Sarro P M, Sinsheimer J, Smedley J, Tao S, Theulings A M and Vuik K 2017 *Nuclear Instruments and Methods in Physics Research Section A: Accelerators, Spectrometers, Detectors and Associated Equipment* **847**(November 2016), 148–161.
URL: *http://linkinghub.elsevier.com/retrieve/pii/S0168900216312311*

van Kessel L and Hagen C W 2020 *SoftwareX* **12**, 100605.
URL: *https://doi.org/10.1016/j.softx.2020.100605*

Vaughan J R M 1989 *IEEE Transactions on Electron Devices* **36**(9), 1963–1967.

Villemant M, Sarrailh P, Belhaj M, Garrigues L and Boniface C 2017 *Journal of Physics D: Applied Physics* **50**(48), aa91af.
URL: *https://doi.org/10.1088/1361-6463/aa91af*

Yakobson A M 1966 *Radiotekhnika i Elektronika* **11**, 1813–1823.